Photoelectrons and solar ionizing radiation at Mars: Predictions versus MAVEN observations

W. K. Peterson, E. M. B. Thiemann, Francis G. Eparvier, Laila Andersson, C. M. Fowler, Davin Larson, Dave Mitchell, Christian Mazelle, Juan Fontenla, J. Scott Evans, et al.

AGU PUBLICATIONS

JGR

Journal of Geophysical Research: Space Physics

RESEARCH ARTICLE
10.1002/2016JA022677

Special Section:
Major Results From the MAVEN Mission to Mars

Photoelectrons and solar ionizing radiation at Mars: Predictions versus MAVEN observations

W. K. Peterson[1], E. M. B Thiemann[1], Francis G. Eparvier[1], Laila Andersson[1], C. M. Fowler[1], Davin Larson[2], Dave Mitchell[2], Christian Mazelle[3,4], Juan Fontenla[5], J. Scott Evans[6], Shaosui Xu[2,7], Mike Liemohn[7], Stephen Bougher[7], Shotaro Sakai[8], T. E. Cravens[8], M. K. Elrod[9,10], M. Benna[9], P. Mahaffy[9], and Bruce Jakosky[1]

[1]LASP, University of Colorado Boulder, Boulder, Colorado, USA, [2]SSL, University of California, Berkeley, California, USA, [3]IRAP, UPS-OMP, Université de Toulouse, Toulouse, France, [4]IRAP, CNRS, Toulouse, France, [5]Northwest Research Associates, Boulder, Colorado, USA, [6]Computational Physics Inc., Springfield, Virginia, USA, [7]Department of Climate and Space Sciences and Engineering, University of Michigan, Ann Arbor, Michigan, USA, [8]Department of Physics and Astronomy, University of Kansas, Lawrence, Kansas, USA, [9]NASA Goddard Space Flight Center, Greenbelt, Maryland, USA, [10]CRESST, University of Maryland, College Park Maryland, USA

Key Points:
- We report Martian photoelectron energy spectra obtained on 19 October 2014
- We compare model energy spectra using observed EUV and XUV irradiances and in situ neutral densities
- We find agreement between models and observations within experimental uncertainties

Correspondence to:
W. K. Peterson,
bill.peterson@lasp.colorado.edu

Citation:
Peterson, W. K., et al. (2016), Photoelectrons and solar ionizing radiation at Mars: Predictions versus MAVEN observations, *J. Geophys. Res. Space Physics*, *121*, 8859–8870, doi:10.1002/2016JA022677.

Received 7 MAR 2016
Accepted 10 AUG 2016
Accepted article online 12 AUG 2016
Published online 1 SEP 2016

Abstract Understanding the evolution of the Martian atmosphere requires knowledge of processes transforming solar irradiance into thermal energy well enough to model them accurately. Here we compare Martian photoelectron energy spectra measured at periapsis by Mars Atmosphere and Volatile Evolution MissioN (MAVEN) with calculations made using three photoelectron production codes and three solar irradiance models as well as modeled and measured CO_2 densities. We restricted our comparisons to regions where the contribution from solar wind electrons and ions were negligible. The two intervals examined on 19 October 2014 have different observed incident solar irradiance spectra. In spite of the differences in photoionization cross sections and irradiance spectra used, we find the agreement between models to be within the combined uncertainties associated with the observations from the MAVEN neutral density, electron flux, and solar irradiance instruments.

1. Introduction

Solar ionizing radiation at wavelengths below about 90 nm incident on the Martian ionosphere and thermosphere is a primary energy source for these regions. Solar irradiance below 90 nm often varies by factors of up to 100 over the solar disk [e.g., *Chamberlin et al.*, 2007, 2008]. Earth and Mars are generally exposed to different ranges of solar longitudes and thus different irradiance below 90 nm. Until the launch of Mars Atmosphere and Volatile Evolution MissioN (MAVEN) there were no systematic observations of the solar irradiance incident on Mars. Consequently, uncertainties in the solar irradiance incident on Mars were significantly larger than those on Earth. By reducing uncertainties in our understanding of the short-wavelength solar irradiance impacting Mars, we can improve our ability to model the Martian atmosphere.

The process of converting solar irradiance to thermal energies begins with photoionization in the Martian thermosphere. A technique for estimating our understanding of this process is to compare observed Martian suprathermal electrons with those calculated by well-tested codes using various estimates of solar irradiance and neutral density. Instruments on the MAVEN now provide broadband solar irradiance data, neutral density data, and suprathermal electron energy spectra that can be used to assess our understanding of solar energy input and our ability to model the production of Martian photoelectrons [*Jakosky et al.*, 2015].

There have been numerous investigations of suprathermal Martian electrons. Initially, they were used to identify field lines coming from the ionosphere as described in the review of *Frahm et al.* [2006]. Recently, *Peterson et al.* [2013] attempted to deduce variations in short-wavelength solar radiation at Mars from variations in suprathermal electron energy spectra observed on the Mars Global Surveyor (MGS) satellite. The MGS survey data used in the 2013 study were acquired well above the primary photoelectron production region, so Peterson and his colleagues developed procedures to identify photoelectrons streaming up magnetic field lines from the primary production altitude between 150 and 200 km. The attempt to use variations in MGS electron spectra to monitor variations in short-wavelength solar irradiance was not successful because of the very small number of intervals of MGS data near 400 km without a significant noise signal from solar wind

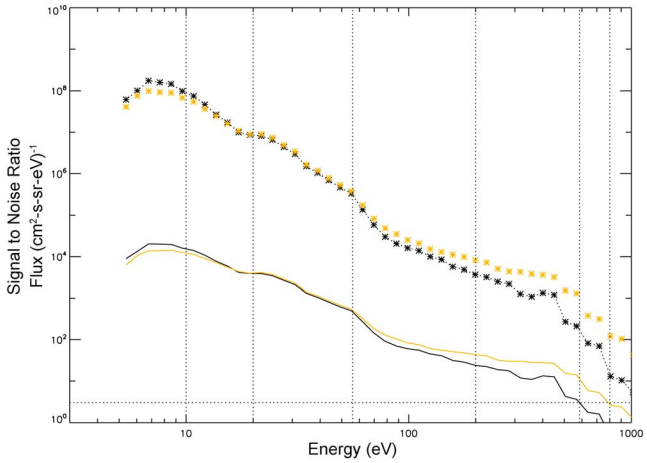

Figure 1. Electron spectra (symbols) and the associated signal-to-noise value (lines) observed on MAVEN before (black) and after (orange) an X class flare that was detected at 05:08 on 19 October 2014. The times and other observational details are given in Table 1. Signal-to-noise ratio (*S/N*) is defined as the ratio of the observed flux to the square root of the associated measurement variance. The dotted horizontal line indicates a *S/N* of 3. Vertical dotted lines are shown at 10, 20, 56, 200, 585, and 800 eV, energies that are noted in the text. Increased fluxes above ~ 56 eV are seen after the flare. The *S/N* ratio is greater than 3 below 585 eV preflare and below 800 eV postflare.

electrons. *Xu et al.* [2015a] compared photoelectron energy spectra calculated using their multistream SuperThermal Electron Transport (STET) model and two different models of solar irradiance. They found that the calculated photoelectron spectra agreed mostly to within a factor of 2. *Sakai et al.* [2015] used a different two-stream code developed at Kansas University (KS) and solar irradiances from the Heliospheric Environment Solar Spectral Radiation (HESSR) model [*Fontenla et al.*, 2009, 2011] to model suprathermal electron observations. The *Sakai et al.* [2015] analysis suggested that differences between the calculations and observations could be explained by reducing the HESSR irradiance in the 30 nm range.

Here we focus on the production of photoelectrons below 200 km, where transport is not a dominant process. We compare and contrast observed suprathermal electron and calculated photoelectron spectra before and after an X class flare that was seen at Mars on 19 October 2014 at 05:08 UT. We use the three photoelectron production codes noted above, modeled and measured neutral densities, and several approaches to model the solar irradiance spectrum at 1 nm resolution before and after the X class flare.

2. Data and Models

2.1. Suprathermal Electron Data

Figure 1 presents two suprathermal electron energy spectra (symbols) and the signal-to-noise ratio (*S/N*, solid lines) of observations obtained on 19 October 2014 before (01:29:36 UT, black) and after (06:04:50 UT, orange) an X class flare that began at 05:08 UT. The omnidirectional data from the MAVEN Solar Wind Electron Analyzer (SWEA) [*Mitchell et al.*, 2016] were acquired over 16 s and have been corrected for the spacecraft potential measured by the Langmuir Probe and Waves instrument on MAVEN (LPW) [*Andersson et al.*, 2015]. The spacecraft potential and other observational parameters for the two times are given in Table 1. Here the signal-to-noise ratio is calculated from the ratio of the observed signal to the square root of its variance. The dotted horizontal line in Figure 1 indicates a *S/N* of 3, the lowest value where uncertainties associated with the detector count rate are negligible. As expected, the fluxes of electrons with energies above ~ 56 eV (shown as the dotted vertical line in Figure 1) are significantly enhanced after the flare because of the increase in solar irradiance at wavelengths shorter than ~17 nm, the so-called aluminum edge in the solar spectrum. Note that unless explicitly stated, the conversion between wavelength and photoelectron energy uses a generic photoionization potential of 15 eV.

Table 1. Observational Details

Time (UT)	Aerocentric Altitude (km)	Solar Zenith Angle (deg)	Geographic Latitude (deg)	Geographic Longitude (deg)	Spacecraft Potential (eV)	Magnetic Dip Angle (deg)
01:29:36	182.5	68.7	48.3	2.4	−2.0	14
06:04:50	194.3	72	50.9	290.6	−2.1	13

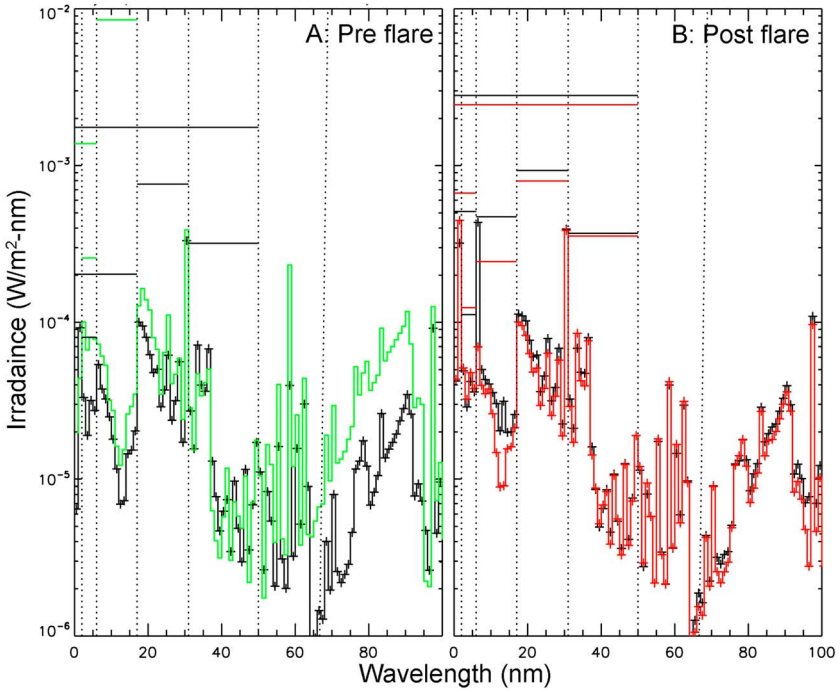

Figure 2. Inferred solar spectral irradiance as a function of wavelength at Mars on 19 October 2014. (a) The preflare values are daily average values from L3D model (black) and HESSR (green). (b) Postflare values at 06:04 are the L3F model (black) and the L3FR model (red). Vertical dotted lines are shown at 2, 6, 17, 31, 50, and 65 nm. Integral irradiance over 0–6, 6–17, 17–31, 31–50, and 0–50 nm are shown as solid lines colored to correspond with the spectra. The spectra in Figure 2a are used for preflare model runs; the spectra in Figure 2b are used in the postflare model runs.

2.2. Solar Data and Models

We use two models of the solar irradiance incident on Mars: (1) the MAVEN Level 3 data product (L3D), which is a modification of the Flare Irradiance Spectral Model (FISM) [*Chamberlin et al*., 2007, 2008] expanded by MAVEN observations [*Eparvier et al*., 2015], and (2) the Heliospheric Environment Solar Spectral Radiation (HESSR) [*Fontenla et al*., 2009, 2011] irradiance model. As noted by *Xu et al*. [2015a] both Martian irradiance spectra models use Earth-based assets but different approaches to account for the temporal and spectral variability of extreme ultraviolet (EUV) and soft X-ray (XUV) irradiance over the solar surface. The HESSR approach is to compute the solar irradiance from the portion of full disk solar EUV images obtained from near-Earth orbit that are visible to an observer on Mars. The other model is derived from MAVEN data and is formally designated the MAVEN R1V2 EUVM Level 3 data product. This data product is available on daily and minute cadences (Level 3 daily: L3D and Level 3 flare: L3F). Both L3D and L3F models use MAVEN broadband irradiance channels in the 0.1–7 nm, 17–22 nm, and 121–122 nm bands [*Eparvier et al*., 2015]. When EUVM measurements are not available, the L3D substitutes with Earth centric measurements, which are interpolated to the solar disk as viewed from Mars. The L3D and L3F products have 1 nm resolution. The L3D product is a median spectrum, which minimizes the biasing caused by including solar flare events. The HESSR spectra have a 1 nm resolution on a daily cadence above 6 nm and 0.05 nm resolution below 6 nm.

Photoelectrons with energies greater than 10 eV are produced by photons with wavelengths shorter than 50 nm. Figure 2 presents models of the solar irradiance spectra from 0 to 100 nm for the preflare and postflare times indicated in Table 1. The black lines in Figure 2a show the L3D spectrum for 19 October 2014. Two versions of the postflare irradiance spectrum are shown in Figure 2b. The black lines are the 1 min cadence L3F model. The red lines show the L3D data product scaled by spectral measurements of preflare/postflare intensity seen at Earth by the Thermosphere, Ionosphere, Mesosphere, Energetics, and Dynamics (TIMED)/Solar Extreme Ultraviolet Experiment (SEE) instrument [*Woods et al*., 1998] and denoted as L3FR below. Vertical dotted lines are shown in Figure 2 at 6, 17, 31, and 50 nm. Integral irradiance over 0–6, 6–17, 17–31, 31–50, and 0–50 nm bands are shown as solid lines colored to correspond with the spectra.

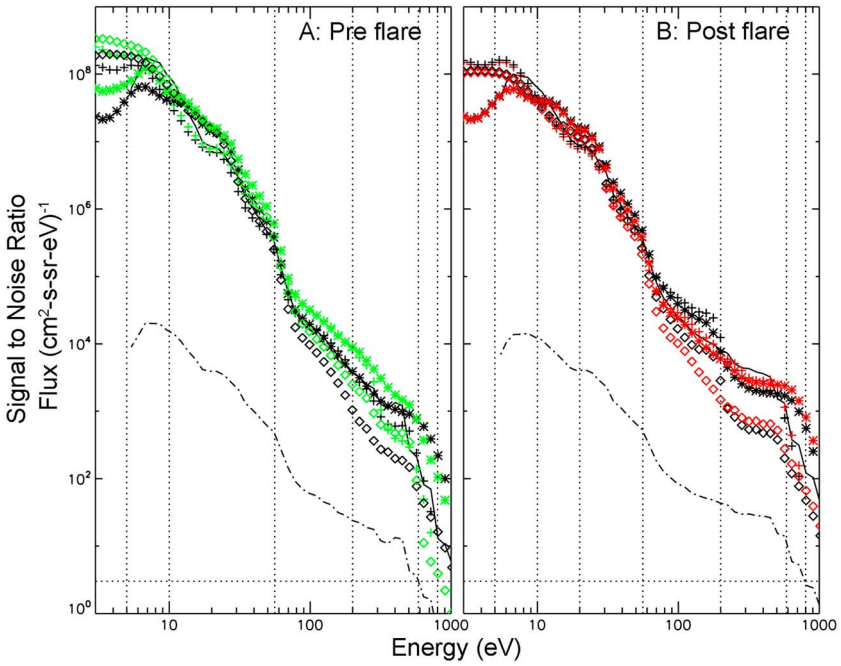

Figure 3. Observed (black lines) and modeled (symbols) electron fluxes for the times given in Table 1. (a) Black symbols show model results using the FISM-M L3D spectrum, and green symbols show model results using the HESSR daily irradiance spectrum. (b) The black symbols are from model runs using the L3F model, and the red symbols are from the L3FR model. Plus symbols show values calculated using the Michigan STET code; asterisks show values calculated using the AURIC code; and open diamond symbols show values calculated using the Kansas two-stream code. Also shown are the *S/N* ratios from Figure 1 (dash-dotted lines), horizontal dotted lines at a *S/N* = 3, and vertical dotted lines at 10, 20, 56, 200, 585, and 800 eV mark boundaries of energies separating different qualities of data-model agreement discussed in the text.

The total solar irradiance incident on Mars is about one half that incident on Earth or ~500 W/m^2. Of that less than 10^{-2} W/m^2 occurs at wavelengths less than 50 nm. The postflare intensification in electron flux at energies above ~56 eV in Figure 1 is produced by solar irradiance below 17 nm shown in Figure 2b. The significant differences between the two irradiance spectra shown in Figure 2a between 56 and 100 nm produce different photoelectron fluxes with energies less than ~6 eV shown in Figure 1. We note also that in the preflare spectra below 50 nm the distribution of intensity differs primarily in the 6–31 nm range where the HESSR irradiance spectrum has about 30% more power than the L3D spectrum. The postflare spectra shown in Figure 2b differ mostly in the 6–17 nm range.

2.3. Neutral Density and Models

The neutral density in the region below 200 km examined here is dominated by CO_2. In situ observations of CO_2 density are available from the MAVEN Neutral Gas and Ion Mass Spectrometer [*Mahaffy et al.*, 2015] and model values that have been validated against many previous Mars missions from the Mars Global Ionosphere-Thermosphere Model (M-GITM) [*Bougher*, 2012; *Bougher et al.*, 2015a]. *Bougher et al.* [2015b] reported agreement within observational uncertainty of ~7% between Neutral Gas and Ion Mass Spectrometer (NGIMS) and M-GITM between 180 and 200 km during a MAVEN deep-dip campaign in April 2015.

Our analysis compares measured and modeled photoelectron energy spectra. In the analysis below we begin by using CO_2 densities from the M-GITM simulation with an Earth $F_{10.7}$ = 130 sfu (solar flux unit; 1 sfu = 10^{-22} W m^{-2} Hz^{-1}). We show section 3 below that the M-GITM model and NGIMS Version 6 CO_2 densities differ by less than 12%.

2.4. Photoelectron Production Codes

To explore the uncertainties in our understanding of solar irradiance energy input to the Martian system using the data and solar irradiance spectra presented above, we use three photoelectron production codes: the University of Michigan STET (Super Thermal Electron Transport) code [*Liemohn et al.*, 2003; *Xu and*

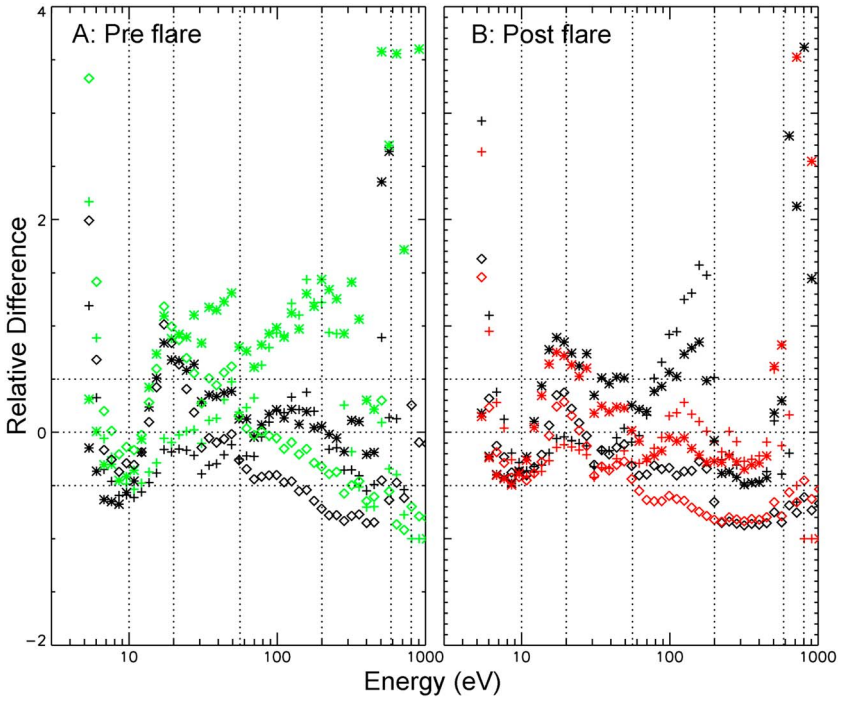

Figure 4. Relative difference between observed and modeled electron flux values as a function of energy shown in Figure 3 . Relative difference = (modeled − observed values)/observed values. The colors and symbols are the same as those used in Figure 3. Horizontal dotted lines are shown at −0.5, 0, and +0.5. Vertical dotted lines are shown at 10, 20, 56, 200, 585, and 800 eV. The signal to noise ratio of the observations is less than three above 585 eV in panel A and above 800 eV in panel B.

Liemohn, 2015; *Xu et al*., 2015a], the University of Kansas two-stream code (denoted as KS below) [*Cravens et al*., 2004; *Sakai et al*., 2015], and the Atmospheric Ultraviolet Radiance Integrated Code (AURIC) [*Strickland et al*., 1999]. These codes incorporate similar sets of photoelectron production cross sections and are commonly used in the study of planetary atmospheres.

In addition to knowledge of the solar irradiance spectrum, these codes also require data on the neutral density and composition. In this initial assessment the AURIC and STET models use neutral density and composition values at latitude 52.5° and longitude 47.5° obtained from the Mars Global Ionosphere-Thermosphere Model (M-GITM) [*Bougher*, 2012; *Bougher et al*., 2015a], from a simulation run with an Earth $F_{10.7} = 130$ sfu. The KS model used slightly different neutral densities. The KS CO_2 densities are identical with the M-GITM model, but the O and CO densities are 30% lower in the KS model. Given that CO_2 is the dominant species below 200 km, these differences do not affect the calculated electron fluxes.

Below we first compare the data and models using the M-GITM model CO_2 densities. We subsequently discuss the implications of the small differences between the M-GITM model and NGIMS Version 6 CO_2 densities.

3. Data-Model Comparison

Figure 3 repeats the observed preflare and postflare electron spectra and signal-to-noise ratio as solid and dash-dotted black lines. The model results have been convolved with an instrument response function [*Mitchell et al*., 2016] to facilitate comparison with observations. Symbols display calculated photoelectron spectra as follows: plus symbols, STET; asteriskd, AURIC; and open diamonds, KS. Model results using the L3D (Figure 3a) and L3F (Figure 3b) models are encoded using black symbols. Green symbols show results calculated using HESSR irradiance values at Mars, and red symbols show values calculated using the L3FR model. Vertical dotted lines are drawn at 10, 20, 31, 56, and 200 eV marking the boundaries of energy bands discussed below. The most striking features in Figure 3 are the agreement between models and observations between about 10 and 56 eV and the disagreement between specific models and observations above and below these energies.

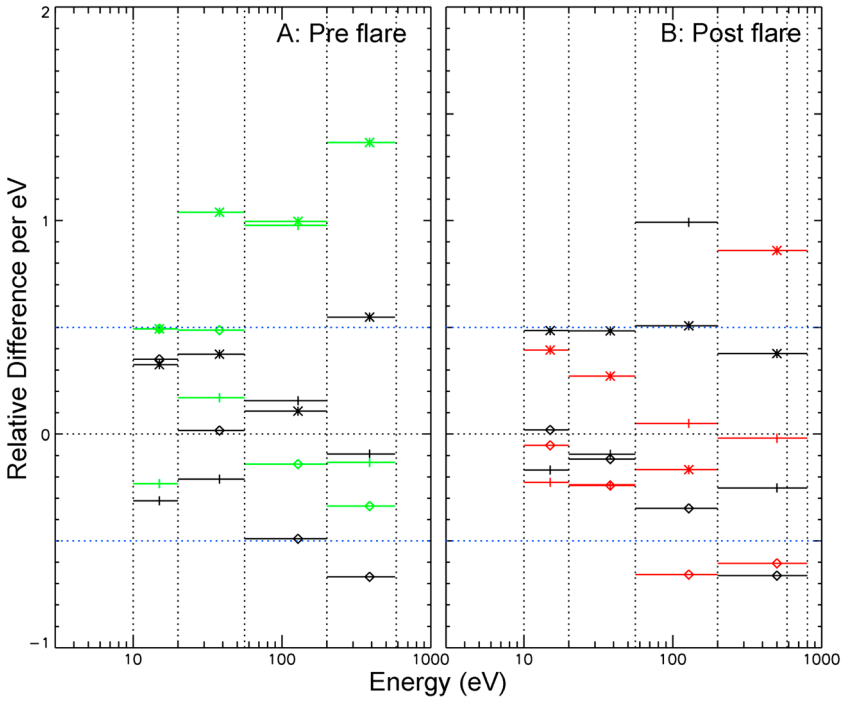

Figure 5. Effective relative difference between models and observations. Energy band integrated relative differences between observations and models using the same symbols and colors used in Figures 2–4.

The large dynamic range of the electron fluxes shown in Figure 3 impedes detailed visual inspection of the agreement between observed and modeled electron spectra. Figure 4 presents an alternative way to display the differences between models and observations. Figure 4 shows the same model calculations presented in Figure 3 that are encoded with the same symbols and colors for comparison with observations. The relative difference reported in Figure 4 is the difference between the modeled and observed fluxes divided by the observed fluxes plotted as a function of energy. A value of 0 (middle dotted horizontal line) indicates model data agreement. A value of ± 0.5 (top and bottom horizontal dotted lines) indicates that the data and models disagree by 50%.

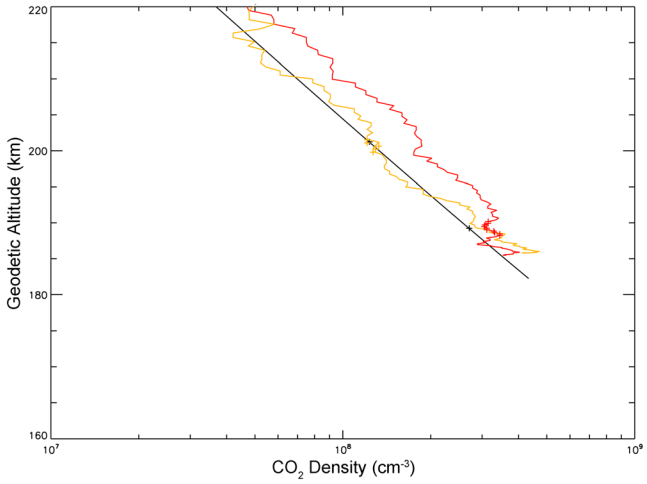

Figure 6. Measured and model CO_2 densities as a function of geodetic altitude. Solid black: CO_2 densities from the M-GITM model data used in the calculations reported in Figures 3–5 discussed above. The black plus symbols indicate the altitudes where the preflare and postflare comparisons were made. Version 6 CO_2 densities observed by NGIMS are shown for the inbound legs of the preflare (red) and postflare (orange) passes. Red and orange plus symbols indicate NGIMS observations within ± 1 km of the altitudes where the preflare and postflare comparisons were made.

The energies indicated by vertical dotted lines in Figure 4 at 10, 20, 56, 200, 575, and 800 eV mark boundaries of different qualities of data-model agreement. Figure 5 presents integrals of the differences over the energy range of each of the four energy bands identified in Figure 4 divided by the width of the band in eV. This could best be called effective difference per eV. The format emphasizes consistent differences over the individual energy bands. Note that the preflare high-energy band in Figure 5a is from 200 to 575 eV and the postflare band in Figure 5b is from 200 to 800 eV. The upper limits

Table 2. Measured and Modeled CO_2 Densities

	Aerocentric Altitude (km)	Geodetic Altitude (km)	NGIMS CO_2 (cm^{-3})	M-GITM CO_2 (cm^{-3})	Ratio
Preflare	182.5	189.2	3.2×10^8	2.9×10^8	0.89
Postflare	194.3	201.2	1.3×10^8	1.3×10^8	0.99

of the high-energy bands are set where the signal-to-noise ratio goes below 3. The results are not significantly different if the upper energy limit shown in Figure 5b is set to 575 eV.

The model runs discussed above used CO_2 densities from the M-GITM model and in section 4 we show that within observational uncertainties, the data and modeled flux intensities agree. These model runs and comparisons were done in aerocentric coordinates which ignore Martian topography. The Neutral Gas and Ion Mass Spectrometer (NGIMS) [*Mahaffy et al*., 2015] measures CO_2 densities in geodetic coordinates. Geodetic altitudes can be as much as 20 km different in the two systems. Figure 6 presents Version 6 of the CO_2 densities reported by NGIMS and the M-GITM values as a function of geodetic altitude. Table 2 shows that the preflare and postflare observed and M-GITM CO_2 densities agree within 11%.

4. Discussion

Observations from the MAVEN spacecraft of suprathermal electrons, neutral densities, and models of broadband solar ionizing radiation incident on Mars from MAVEN presented above provide an opportunity to asses our understanding of processes heating the Martian thermosphere and ionosphere. We perform this assessment by comparing observations with photoelectron spectra calculated from three independent codes using multiple models of solar irradiance before and after an X class flare. The model calculations were made using M-GITM model CO_2 densities. Figure 6 shows the small (12%) difference between the M-GITM and Version 6 NGIMS level 2 values.

4.1. Observational Uncertainties

Uncertainties in the observed electron spectra arise from natural and instrumental sources. Instrumental sources include uncertainties in calibration, systematic biases in the energy response, and uncertainties associated with finite counting rates. The signal-to-noise ratio shown in Figure 1 is > 3 below 575 eV before the flare and below 800 eV after the flare. The uncertainties associated with finite counting rates are not important below these energies. *Mitchell et al*. [2016] have cross calibrated with other MAVEN instruments, including plasma densities measured by the LPW instrument [*Andersson et al*., 2015]. They estimate that the absolute calibration of the SWEA is accurate to within 25%. The energy response of the MAVEN SWEA instrument is set by the electron optics-associated top hat design and is directly related to the uniformity of the separation of the deflector plates [*Carlson et al*., 2001]. The magnitude of the uncertainty associated with sensor plate misalignment is negligible compared to the absolute calibration.

There are two natural sources of noise in the Martian ionosphere that could contribute to the electron spectra considered here: penetrating solar wind electrons and penetrating solar wind ions. A characteristic of penetrating solar wind electrons is the antisunward directed angular distribution. We examined electron angular distributions at the times indicated in Table 1 and found anisotropic distributions before and after the intervals of interest when the spacecraft was at higher altitudes. The spectra reported in Figure 1 were found to be isotropic, and thus the electron spectra reported in Figure 1 are not contaminated by penetrating solar wind electrons. *Halekas et al*. [2015] found and reported an unexpected signature of penetrating solar wind protons in the MAVEN Solar Wind Ion Analyzer (SWIA) at altitudes in the range sampled here. Halekas et al. demonstrated that solar wind protons charge exchange with the neutral hydrogen corona and are transported to lower altitudes where they again charge exchange to produce beams of protons (H^+) at the solar wind velocity and in the direction of the solar wind. A small flux of directed H^- is also produced by electron attachment that converts neutral H to H^- with approximately the same energy and direction as the H^+ produced by electron stripping. We examined ion energy distributions from the SWIA instrument at the times indicated in Table 1. We found evidence of solar wind H^+ beams but at energies above 1 keV. We conclude that the spectra shown in Figure 1 are produced by photoionization and are not contaminated by penetrating solar wind electrons or H^- produced by penetrating solar wind protons.

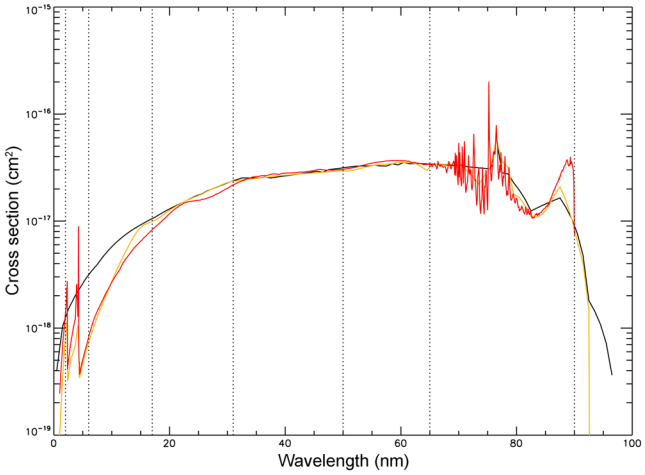

Figure 7. Total CO_2 photoionization cross sections as a function of wavelength used in the photoelectron production codes. The cross sections are color coded as follows STET: black, KS: orange, and AURIC: red. The vertical dotted lines are at 2, 6, 17, 31, 50, 65, and 90 nm.

Uncertainties in the solar ionizing radiation incident on Mars can be estimated by analysis of independent models of the preflare and postflare irradiance spectra below ~50 nm shown in Figure 2. The data shown in Figure 2 show that the preflare integrated power below 50 nm from the HESSR model is about 30% greater than that from the MAVEN Level 3 daily data product. *Chamberlin et al.* [2007] report uncertainty below ~30 nm of ~30% for the Earth centric FISM irradiance model, from which the MAVEN Level 3 data products are derived. The two postflare irradiance spectra shown in Figure 2b use two different methods to estimate the enhancements in the EUVM Level 3 daily data product associated with the flare and agree better than the preflare spectra. *Chamberlin et al.* [2008] report slightly larger uncertainties in the FISM irradiance model during flares, approaching 100% at some wavelengths and well above the differences seen in Figure 2b at all wavelengths. We conclude that the Martian preflare and postflare irradiance models agree within the uncertainties of the models, i.e., ~ 30% preflare and ~50% postflare.

The M-GITM model densities used here were derived from prior Mars missions and extrapolated to lower altitudes. The NGIMS Version 6 observations shown in Figure 6 have been adjusted from previous versions to account for densities derived using MAVEN accelerometer data [*Zurek et al.*, 2015]. Uncertainties in the measured CO_2 density are estimated at 30%. Table 2 shows that the M-GITM density used in the preflare calculation agreed to within 11% of the measured value, and the postflare value agreed to within 1%.

The calculation of photoelectron energy spectra shown in Figure 3 involves modeling the processes of photoionization, transport, and secondary ionization by energetic photoelectrons. The photoelectron production and transport codes used to produce the photoelectron spectra shown in Figure 3 all use the CO_2 neutral density obtained from the Mars Global Ionosphere-Thermosphere Model (M-GITM) [*Bougher*, 2012; *Bougher et al.*, 2015a]. The uncertainties associated with these calculations include the following: the absolute uncertainties in solar irradiance (30% to 50% for daily values and $<$ 100% for flares), the uncertainties in the neutral density (30%), and the uncertainties in photoionization and electron impact ionization cross sections (discussed below).

The photoelectron production codes used here include transport effects, but at ~190 km where the calculations are made transport is not a dominant process. The mean free path of electrons is about 1.5 km and with only a modest (± 0.5 km) variation over the 1 to 1000 eV energy range considered.

Assuming the observational uncertainties are not correlated, the total observational uncertainty from SWEA, EUVM, and NGIMS observations is 65% preflare and 110% postflare. Ignoring other uncertainties, this means that the agreement between observations and calculated electron spectra better than this is not significant.

4.2. Photoionization and Electron Impact Ionization Cross Sections

We continue our detailed comparison of the model/data differences shown in Figure 3 by considering the cross sections used in the STET, KS, and AURIC codes. Figure 7 presents the photoionization cross sections for CO_2 as a function of wavelength. The STET code uses the lowest-resolution cross section from *Fox* [1991] colored black; the KS code uses cross sections from *Gan and Cravens* [1990, and references therein] colored orange; and the AURIC code uses the highest resolution cross section colored red. It should be noted that the reason for the higher-resolution cross sections in the AURIC code is because this level of resolution is required to model EUV photoemissions in planetary atmospheres [*Strickland et al.*, 1999], which is the primary

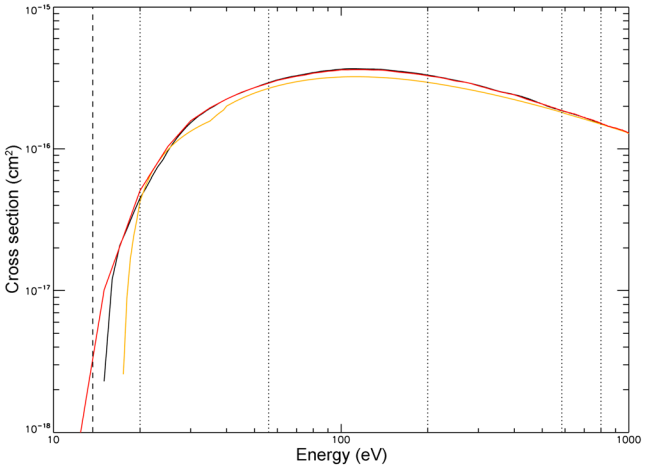

Figure 8. Total CO_2 electron impact ionization cross sections as a function of wavelength used in the photoelectron production codes. The cross sections are color coded as follows STET [from *Fox and Sung*, 2001]: black, KS [from *Gan and Cravens*, 1990, and references therein]: orange, and AURIC: red. The vertical dashed line at 13.7 eV denotes the ionization threshold for CO_2. Vertical dotted lines are also shown at 20, 56, 200, 585, and 800 eV.

use of the AURIC code. All cross sections show a broad peak from 30 to ~70 nm. Below ~17 nm the cross sections used by the AURIC and KS codes are significantly lower than that used by the STET code, except for the Auger photoionization features at 2.2 and 4.4 nm, corresponding to electrons of 500 and 250 eV, respectively [e.g., *Moddeman et al.*, 1971], which are not included in the STET code. The STET code, however, includes the double ionization cross sections for CO_2 which are not shown in Figure 7.

Photoionization by solar irradiance shorter than 42 nm produces electrons with enough energy to ionize CO_2 and create secondary electrons. These secondary electrons are part of the observed suprathermal electron energy spectrum. The photoelectron codes used here capture this component of the photoelectron spectra. Figure 8 presents the electron impact ionization cross sections for CO_2 used by the three codes noted above. The cross sections peak at ~ 100 eV where the one used by the KS code is about 20% lower. The falloff in cross section value below 20 eV is qualitatively different for the three codes. The AURIC cross section extends below the CO_2 ionization potential (13.7 eV) reflecting the fact that the cross sections used in the AURIC code include electron impact ionization of excited states of CO_2.

Differences of the spectral resolution of the photoionization cross sections shown in Figure 7 will have the largest impact on the calculated photoelectron flux where there is structure in the cross sections, i.e., below 6 nm and above 65 nm corresponding to electrons with energies greater than 200 eV and less than 5 eV, respectively. Differences in the magnitude of the electron impact cross sections will impact the calculated photoelectron spectra for wavelengths longer than ~35 nm which produce secondary electrons with energies less than 20 eV. We cannot make a data-model comparison for ionization produced by wavelengths greater than 65 nm because observations extend only to 5 eV in the plasma frame of reference.

4.3. Detailed Data/M-GITM-Based Model Comparisons

The relative difference between modeled and observed electron spectra is defined as ((model flux − observed flux)/observed flux). Figure 4 presents the relative differences as a function of energy. Figure 5 presents them for four selected energy bands. Values of ± 0.5 (top and bottom horizontal dotted lines) indicate that the data and models disagree by 50%. Positive values indicate that the modeled fluxes are larger than the observations. In general, the disagreement between models and data between 5 and 800 eV is less than 50%, i.e., within uncertainties associated with the data. The agreement between data and models is, however, not uniform in energy. In the sections below we address differences in three broad energy ranges

4.3.1. Energies Above 200 eV

The photoelectron spectra calculated with all three codes agree remarkably well with observations above 200 eV. Figure 5 shows that the model fluxes, on average, agree best with those calculated using the STET code above 200 eV. The fluxes from the AURIC code are higher, and those from the KS code are lower. Two codes (AURIC and KS) make some provision for calculating the effects of the narrow Auger electron lines near 250 and 500 eV. We consider preflare and postflare data-model comparisons separately.

Postflare, the differences in the two irradiance spectra below 6 nm are mostly in the 2 nm bin which produces electrons with energies that are detected in the energy channel centered on 568 eV and include a contribution from Auger electrons near 500 eV. In the region around the 250 eV Auger line the AURIC and STET codes agree quite well with the data and the KS code predicts systematically lower fluxes. Agreement between the

codes and data in the 505 and 568 eV energy channels is different. The AURIC code predicts significantly higher fluxes than those observed, while the KS and STET codes give about the same agreement with observations that were seen near the 250 eV Auger line. The KS code predicts lower electron fluxes than those observed. This reflects the lower value of the photoionization cross section compared to the STET code and lower energy resolution compared to the AURIC code.

Figure 2 shows that the preflare L3D and HESSR integrated irradiance power below 6 nm is about the same, but the distributions in wavelength are different. The L3D irradiance values peak in the 1 nm bin, whereas the HESSR values are approximately uniform in intensity from 2 to 6 nm. Both postflare irradiance spectra below 6 nm in Figure 2b have the same shape as the L3D irradiance spectra shown in Figure 2a. Preflare data-model agreement using L3D irradiance spectra (black symbols in Figure 4a) is similar to postflare agreement shown in Figure 4b. Here again the AURIC code predicts significantly higher fluxes than observed. Preflare data-model comparisons made using the HESSR irradiance spectra are shown as green symbols in Figure 4a. We see that the AURIC code again predicts significantly more electron flux over most of the energy steps sampled above 200 eV. Between 200 and 400 eV this reflects the significantly more intense HESSR irradiance spectra between 2 and 6 nm. The preflare agreement between the KS code is similar to the postflare case. We note that *Moddeman et al*. [1971] do not report C, N, or O Auger electron emission lines above ~500 eV. Because the AURIC code predicts significantly higher fluxes than are observed in both the 505 and 568 eV channels, the treatment of Auger features in the cross sections cannot explain the disagreement.

It is interesting to note that the AURIC code, which uses the highest resolution photoelectron production cross section, systematically overestimates the observed electron fluxes. The irradiance spectra below 6 nm used here are derived from model-dependent distributions of power observed in a broad wavelength region. Figure 2 shows the significant differences in modeled irradiance spectra in this region. *Peterson et al*. [2012] found that the variability of solar irradiance below 8 nm was not fully captured in any of the irradiance models they considered. We do not have the information to determine if the systematic overestimation of photoelectron fluxes above 600 eV arises from imperfect knowledge of the photoionization cross sections or imperfect knowledge of the solar irradiance spectrum below 6 nm.

4.3.2. Energies Between 20 and 200 eV

In spite of the significant differences in irradiance spectra and photoionization cross sections relevant to energies in the 20 to 200 eV range, the photoelectron spectra calculated with all three codes agree remarkably well with observations. Figure 5 shows that on average and within observational uncertainty, the calculated photoelectron energy spectra between 20 and 200 eV are within 50% of the observations with three exceptions. The exceptions are preflare fluxes calculated using the AURIC/HESSR pair, preflare and postflare fluxes calculated using the STET/HESSR and STET/L3D pair, and postflare fluxes calculated using the KS/L3FR pair. Examination of the highest-energy resolution data in Figure 4 show that the exceptions reflect the systematically different energy responses calculated in the 20 to 200 eV range.

The data/KS model agreement decreases systematically from ~56 eV to over 200 eV (which corresponds to photons with wavelengths between 6 and 17 nm) for all cases examined. These systematic variations with energy are associated with the systematic decrease in magnitude of the photoionization cross section (orange line in Figure 7) below ~30 nm. The response of the STET and AURIC codes from 56 to 200 eV are more complicated. The systematic decrease seen in the data/KS model agreement appears near 200 eV in the preflare STET and AURIC models using the L3D and postflare STET and AURIC models using the L3FR irradiance spectra.

In contrast to the systematic decreases in data/model agreement noted above, there is a systematic increase near 200 eV for the STET and AURIC data/model agreement using the preflare HESSR irradiance and postflare L3F irradiance spectra. The more intense irradiance features near 6 nm in the HESSR and L3F irradiance spectra apparently are strong enough to overcome decreases in the photoionization cross sections.

4.3.3. Energies Below 20 eV

Figure 5 shows that the data/model agreement in the 10–20 eV range is within observational uncertainties for all model/irradiance spectra pairs examined. Data are available for comparison with the models only above ~5 eV, which is the lowest SWEA energy step plus the spacecraft potential. Figure 4 shows that the data/model agreement within observational uncertainties extends to 5 eV for the AURIC code but not the KS and STET codes. Electrons with energies in the 5 eV range can be produced by photons with wavelengths

near 65 nm, where the cross section for photoionization has many features associated with the production of excited states of CO_2. The AURIC code is routinely used to investigate optical emissions from ionized plasmas and has been extensively validated [*Strickland et al*., 1999] in this energy/wavelength range.

5. Data-Model Comparison Using Observed CO_2 Densities

The model photoelectron fluxes presented and discussed above were all calculated using the M-GITM model CO_2 density shown in Figure 6. Table 2 shows that the postflare CO_2 densities from the NGIMS instrument and M-GITM agree to within 1%, so postflare electron fluxes are unchanged. The preflare CO_2 densities at the measurement altitude observed by the NGIMS instrument are 11% higher than the M-GITM values.

Xu et al. [2015b] have shown that in collision-dominated regions the flux of high-energy electrons is surprisingly insensitive to neutral density. A test run of the STET code with double the M-GITM density showed a factor of less than 2 increase in the electron flux at 1 eV but essentially no change above 10 eV. Thus, the comparisons between modeled and observed fluxes for the energy bands shown in Figure 5 are not changed when observed CO_2 densities are considered.

6. Conclusion

We examined electron data obtained on successive MAVEN passes with different incident solar EUV and XUV irradiances. We then compared observed and modeled electron spectra based on observed irradiance and CO_2 density. The discussion above shows that in spite of large differences in photoionization cross sections and irradiance spectra incident on Mars, the differences in Martian photoelectron energy spectra calculated with three commonly used codes (i.e., KS, AURIC, and STET) are small compared to the combined uncertainties of observations from the SWEA, NGIMS, and EUVM instruments on the MAVEN spacecraft.

The most significant differences were found for photoelectrons with energies above ~600 eV and below ~5 eV. The Atmospheric Ultraviolet Radiance Integrated Code (AURIC) best agreed with data below ~5 eV. The SuperThermal Electron Transport (STET) code and a two-stream code developed at Kansas University best agreed with data above ~600 eV. Between 200 and 600 eV the lower photoionization cross section used in the KS code results in calculated photoelectron fluxes less than 50% below those observed. We do not have the information to determine if the more than 50% overestimation of photoelectron fluxes above 600 eV by the AURIC code arises from imperfect knowledge of the photoionization cross sections or imperfect knowledge of the solar irradiance spectrum below 6 nm.

Acknowledgments
We thank the MAVEN team for providing spacecraft instruments capable of returning the exceptionally good data used in this report. Input values used for the models are available on request from the lead author. Work related to observations with the SWEA instrument was partially supported by CNES. This research was supported by NASA's Planetary Science Division.

References

Andersson, L., R. E. Ergun, G. T. Delory, A. Eriksson, J. Westfall, H. Reed, J. McCauly, D. Summers, and D. Meyers (2015), The Langmuir Probe and Waves (LPW) instrument for MAVEN, *Space Sci. Rev.*, doi:10.1007/s11214-015-0194-3.

Bougher, S. W. (2012), Coupled MGCM-MTGCM Mars thermosphere simulations and resulting data products in support of the MAVEN mission, JPL/CDP Rep., pp. 1–9, 6 Aug.

Bougher, S. W., D. Pawlowski, J. M. Bell, S. Nelli, T. McDunn, J. R. Murphy, M. Chizek, and A. Ridley (2015a), Mars Global Ionosphere-Thermosphere Model: Solar cycle, seasonal, and diurnal variations of the Mars upper atmosphere, *J. Geophys. Res. Planets*, *120*, 311–342, doi:10.1002/2014JE004715.

Bougher, S., et al. (2015b), Early MAVEN deep dip campaign reveals thermosphere and ionosphere variability, *Science*, *350*, doi:10.1126/science.aad0459.

Carlson, C. W., J. P. McFadden, P. Turin, D. W. Curtis, and A. Magnoncelli (2001), The electron and ion plasma experiment for FAST, *Space Sci. Rev.*, *98*, 33–66, doi:10.1023/A:1013139910140.

Chamberlin, P. C., T. N. Woods, and F. G. Eparvier (2007). Flare irradiance spectral model (FISM): Daily component algorithms and results, *Space Weather*, *5*, S07005, doi:10.1029/2007SW000316.

Chamberlin, P. C., T. N. Woods, and F. G. Eparvier (2008), Flare irradiance spectral model (FISM): Flare component algorithms and results, *Space Weather*, *6*, S05001, doi:10.1029/2007SW000372.

Cravens, T. E., J. Vann, J. Clark, J. Yu, C. N. Keller, and C. Brull (2004), The ionosphere of Titan: An updated theoretical model, *Adv. Space Res.*, *33*, 212, doi:10.1016/j.asr.2003.02.012.

Eparvier, F. G., P. C. Chamberlin, T. N. Woods, and E. M. B. Thiemann (2015), The solar extreme ultraviolet monitor for MAVEN, *Space Sci. Rev.*, doi:10.1007/s11214-015-0195-2.

Fontenla, J. M., E. Quemerais, I. Gonzalez Hernandez, C. Lindsey, and M. Haberreiter (2009), Solar irradiance forecast and far-side imaging, *Adv. Space Res.*, *44*, 457, doi:10.1016/j.asr.2009.04.010.

Fontenla, J. M., J. Harder, W. Livingston, M. Snow, and T. Woods (2011), High-resolution solar spectral irradiance from extreme ultraviolet to far infrared, *J. Geophys. Res.*, *116*, D20108, doi:10.1029/2011JD016032.

Fox, J. L. (1991), Cross sections and reaction rates of relevance to aeronomy, *Rev. Geophys.*, *29*, 1110–1131.

Fox, J. L., and K. Y. Sung (2001), Solar activity variations of the Venus thermosphere/ionosphere, *J. Geophys. Res.*, *106*, 21,305, doi:10.1029/2001JA000069.

Frahm, R. A., et al. (2006), Locations of atmospheric photoelectron energy peaks within the Mars environment, *Space Sci. Rev.*, *126*, 389–402, doi:10.1007/s11214-006-9119-5.

Gan, L., and T. E. Cravens (1990), Electron energetics in the inner coma of comet Halley, *J. Geophys. Res.*, *95*, 6285–6303, doi:10.1029/JA095iA05p06285.

Halekas, J. S., et al. (2015), MAVEN observations of solar wind hydrogen deposition in the atmosphere of Mars, *Geophys. Res. Lett.*, *42*, 8901–8909, doi:10.1002/2015GL064693.

Jakosky, B. M., J. M. Grebowsky, J. G. Luhmann, and D. A. Brain (2015), Initial results from the MAVEN mission to Mars, *Geophys. Res. Lett.*, *42*, 8791–8802, doi:10.1002/2015GL065271.

Liemohn, M. W., D. L. Mitchell, A. F. Nagy, J. L. Fox, T. W. Reimer, and Y. Ma (2003), Comparisons of electron fluxes measured in the crustal fields at Mars by the MGS magnetometer/electron reflectometer instrument with a *B* field-dependent transport code, *J. Geophys. Res.*, *108*(E12), 5134, doi:10.1029/2003JE002158.

Mahaffy, P., et al. (2015), The Neutral Gas and Ion Mass Spectrometer on the Mars Atmosphere and Volatile Evolution Mission, *Space Sci. Rev.*, *195*, 49, doi:10.1007/s11214-014-0091-1.

Mitchell, D. L., et al. (2016), The MAVEN solar wind electron analyzer (SWEA), *Space Sci. Rev.*, *34*, doi:10.1007/s11214-015-0232-1.

Moddeman, W. E., T. A. Carlson, M. O. Krause, B. P. Pullen, W. E. Bull, and G. K. Schweitzer (1971), Determination of the *K—LL* Auger Spectra of N_2, O_2, CO, NO, H_2O, and CO_2, *J. Chem. Phys.*, *55*, 2371, doi:10.1063/1.1676411.

Peterson, W. K., T. N. Woods, J. M. Fontenla, P. G. Richards, P. C. Chamberlin, S. C. Solomon, W. K. Tobiska, and H. P. Warren (2012), Solar EUV and XUV energy input to thermosphere on solar rotation time scales derived from photoelectron observations, *J. Geophys. Res.*, *117*, A05320, doi:10.1029/2011JA017382.

Peterson, W. K., D. A. Brain, D. L. Mitchell, S. M. Bailey, and P. C. Chamberlin (2013), Correlations between variations in solar EUV and soft X-ray irradiance and photoelectron energy spectra observed on Mars and Earth, *J. Geophys. Res. Space Physics*, *118*, 7338–7347, doi:10.1002/2013JA019251.

Sakai, S., A. Rahmati, D. L. Mitchell, T. E. Cravens, S. W. Bougher, C. Mazelle, W. K. Peterson, F. G. Eparvier, J. M. Fontenla, and B. M. Jakosky (2015), Model insights into energetic photoelectrons measured at Mars by MAVEN, *Geophys. Res. Lett.*, *42*, 8894–8900, doi:10.1002/2015GL065169.

Strickland, D. J., J. Bishop, J. S. Evans, T. Majeed, P. M. Shen, R. J. Cox, R. Link, and R. E. Huffman (1999), Atmospheric Ultraviolet Radiance Integrated Code (AURIC): Theory, software architecture, inputs, and selected results, *J. Quant. Spectros. Radiat. Transfer*, *62*, 689, doi:10.1016/S0022-4073(98)00098-3.

Woods, T., F. Eparvier, S. Bailey, S. C. Solomon, G. Rottman, G. Lawrence, R. Roble, O. R. White, J. Lean, and W. K. Tobiska (1998), TIMED solar EUV Experiment, *SPIE Proc.*, *3442*, 180.

Xu, S., and M. W. Liemohn (2015), Superthermal electron transport model for Mars, *Earth Space Sci.*, *2*, 47–64, doi:10.1002/2014EA000043.

Xu, S., M. W. Liemohn, W. K. Peterson, J. Fontenla, and P. Chamberlin (2015a), Comparison of different solar irradiance models for the superthermal electron transport model for Mars, *Planet. Space Sci*, doi:10.1016/j.pss.2015.09.008, in press.

Xu, S., M. Liemohn, S. Bougher, and D. Mitchell (2015b), Enhanced carbon dioxide causing the dust storm-related increase in high-altitude photoelectron fluxes at Mars, *Geophys. Res. Lett.*, *42*, 9702–9710, doi:10.1002/2015GL066043.

Zurek, R., R. H. Tolson, D. Baird, M. Z. Johnson, and S. W. Bougher (2015), Application of MAVEN accelerometer and attitude control data to Mars atmospheric characterization, *Space Sci. Rev.*, *195*, 303, doi:10.1007/s11214-014-0095-x.